The HERMES Back Drift Chambers

S. Bernreuther [a], A.B. Borissov [b 1 2], H. Böttcher [b], S. Brons [b], W. Brückner [c], A. Buchsteiner [b 3], M. Ferstl [a], Y. Gaerber [b], A. Gute [a], U. Harder [b], D. Hasch [b], M. Kirsch [a 4], B. Krause [b 2], W.A. Lachnit [a], F. Meißner [b], G. Modrak [b], F. Neunreither [a], W.–D. Nowak [b], M. Pohl [b], K. Rith [a], H.O. Roloff [b], H. Russo [a], F. Schmidt [a], A.E. Schwind [b], W. Wander [a 5]

[a] *Universität Erlangen–Nürnberg, 91058 Erlangen, Germany*
[b] *DESY-IfH Zeuthen, 15735 Zeuthen, Germany*
[c] *MPI für Kernphysik, 69029 Heidelberg, Germany*
[1] *on leave of absence from State University Saratow, Russia*
[2] *now at DESY, Deutsches Elektronen Synchrotron, 22603 Hamburg, Germany*
[5] *now at Universität Potsdam, 14415 Potsdam, Germany*
[4] *now at Firma "Dr. Bernd Struck", 22889 Tangstedt, Germany*
[5] *now at MIT, Cambridge, MA 02139, USA*

Abstract

The tracking system of the HERMES spectrometer behind the bending magnet consists of two pairs of large planar 6-plane drift chambers. The design and performance of these chambers is described. This description comprises details on the mechanical and electronical design, information about the gas mixture used and its properties, results on alignment, calibration, resolution, and efficiencies, and a discussion of the experience gained through the first three years of operation.

1 Introduction

The HERMES apparatus is based on a forward spectrometer with an internal gas target in the HERA lepton ring to investigate the spin structure of the nucleon by measuring doubly polarised lepton-nucleon scattering. A complete description of the HERMES spectrometer can be found in [1]. The HERMES internal gas target is described in [2].

The apparatus is divided into two halves installed above and below the HERA beam pipes. Each spectrometer half is equipped with the same sequence of detectors. In front of the bending magnet the tracking system is composed of two 3-plane microstrip gas counters just behind the target, a small 6-plane drift chamber that was commissioned in the third year of running, and a pair of 6-plane drift chambers near the magnet. Three proportional chambers are mounted within the gap of the magnet. They are used in the reconstruction of low momentum tracks that do not pass the magnet completely. Behind the magnet, tracking is based upon two pairs of large 6-plane drift chambers, the Back Chambers (BC).

The arrangement of the BCs within the HERMES apparatus is shown in Fig. 1. Each track in the standard spectrometer acceptance behind the magnet is measured by up to 24 individual planes (up to 8 for each of the 3 wire orientations), providing high redundancy. The most upstream pair of BCs contributes also to the momentum determination for some of the short tracks, i.e. tracks that leave the spectrometer prematurely behind the magnet due to their low momentum.

Particle identification is accomplished by a threshold Cherenkov counter, a transition radiation detector, a preshower counter, and an electromagnetic calorimeter, all located behind the magnet. By combining the responses of these detectors, leptons and hadrons can be distinguished in the data analysis.

First results obtained from a test beam exposure of single BC modules have already been published elsewhere [3, 4]. Here further details on the construction of the Back Chambers and their performance in the experiment will be given.

First data was taken in 1995 utilizing a polarised ^{3}He target, which to a good approximation can be considered as a polarised neutron target. In 1996 the target was changed to polarised H, which was used throughout 1997 to investigate the spin structure of the proton. All results presented here are based on data taken in these first three years of running.

2 Mechanical Design

The chamber modules consist of three pairs of wire planes with alternating sense and potential wires between cathode foils. Both the sense wire and cathode foil frames are made of GFK (glass fiber-reinforced epoxy) by Stesalit (Zullwill, Switzerland) with a thickness of 8 mm. Together with the sense wire spacing of

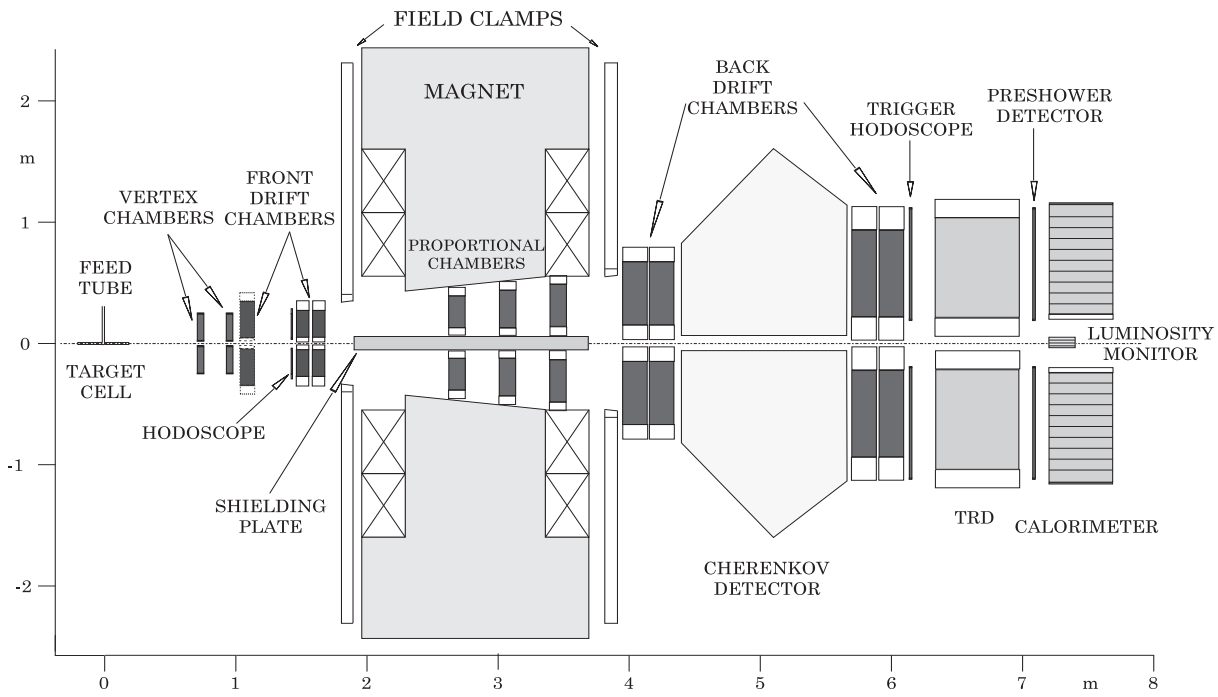

Figure 1: Schematic diagram of the HERMES spectrometer (side view).

15 mm, this leads to an almost square drift cell of size (15 mm x 16 mm). The potential wires and cathode foils are at negative high voltage of typically 1770 V, and the anode wires are at ground potential. The wires are oriented vertically for the x–planes and at an angle of $\pm 30^\circ$ to the vertical for the u– and v–planes. The frames have sufficient length to allow both ends of all wires in the u– and v–planes to terminate on the long edges of the frames. Hence all u– and v–wires have the same length. To help solve the left–right ambiguities, the planes of each pair are staggered by half a drift cell.

A high precision in wire placement is guaranteed by locating pins made of polyoxymethylene. These pins are installed into the GFK-frame along a curved locus that is deflected into a straight line by prestressing before mounting the wires and foils. Therefore the expected stress deflection of the frames caused by the wires and foils is compensated in order to prevent displacement of the u– and v–wires. All wire positions were measured by an optical surveying system built for this purpose and were found to deviate less than 30 μm from the nominal positions [5]. A special wire running beneath a layer of GFK along one long side of each wire frame and crossing under all signal traces provides capacitive coupling of test pulses to check all channels of this plane. To avoid surface currents between the soldering pads for signal and potential wires, a meander shaped groove is machined between these pads. This can be seen in Fig. 2, where

the position pins and the soldering pads are also visible.

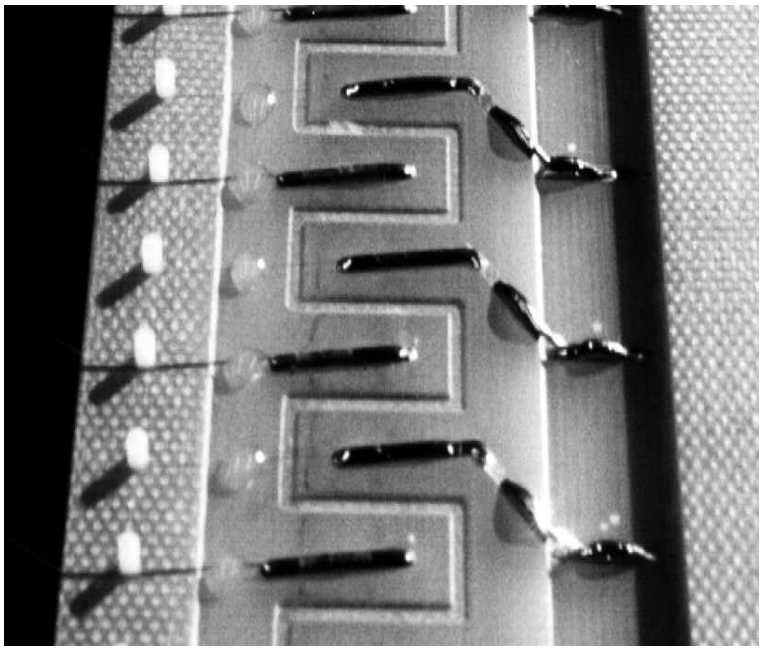

Figure 2: Picture of the soldering pads and positioning pins for the signal and potential wires. Seen also are the meander shaped groove between the pads and the connection of the signal wires to the readout line running beneath a GFK layer.

A schematic view of a complete BC module is shown in Fig. 3. In order to cover the HERMES vertical acceptance extending down to 40 mrad, the active areas of the drift chambers had to be brought close to the beam pipe. This is achieved by scallops in the frames for the beam pipes, as can be seen in Fig. 3. An additional requirement was the rotational symmetry of the chambers around the lepton beam pipe, so that each module can be mounted in the upper or in the lower half of the spectrometer while retaining the same wire orientation. This is the reason for the third scallop also seen in Fig. 3. To guarantee the necessary stiffness and stability of the modules, the GFK–frames are mounted between two 38 mm thick frames made of non–magnetic steel. The exact relative positioning of the wire planes is defined by six steel bolts, each of 45 mm diameter, which run through the stack of planes and are fixed in the steel frames.

As the gas mixture used (see sect. 4) is heavier than air, the gas stream into the chambers is directed from the bottom to the top diagonally through the chambers (see Fig. 3). The gas seal is realized by O–rings made of neoprene–caoutchouc, between all frames. To guarantee a smooth surface for this seal, the signal wire traces pass under a GFK layer (see Fig. 2). The gas leak rates are in the range expected from diffusion through the window foils.

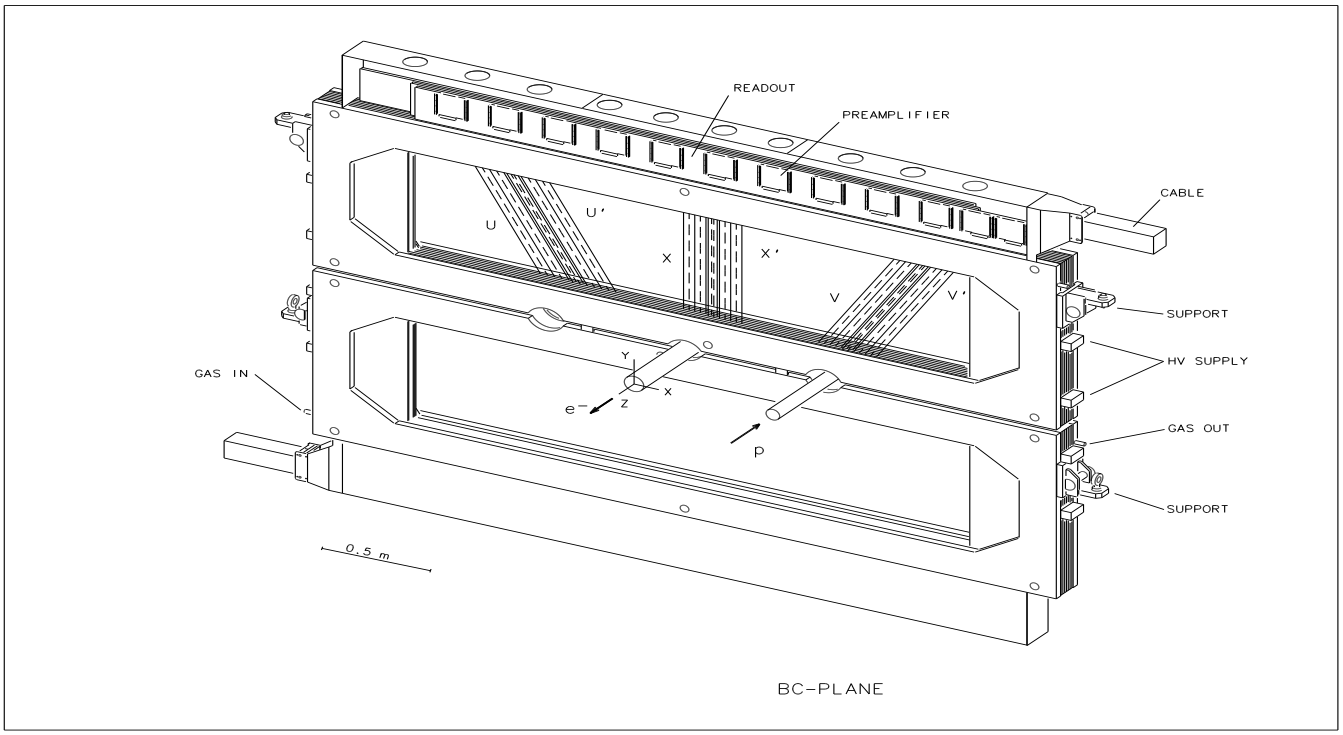

Figure 3: Schematic view of the HERMES BC module.

The spectrometer layout requires two different sizes of BCs, the smaller BC1/2 and the bigger BC3/4. The essential parameters of both types are summarized in Table 1.

Table 1. Back chamber properties

Module active area (mm^2)	1880 × 520	2890 × 710
Sense wires per plane	128	192
Channels per module	768	1152
Cell width × gap	15 mm × 16 mm	
Anode wires	25.4 μm Au coated W	
Potential wires	127 μm Au coated Cu-Be	
Cathode foils	25 μm C coated Kapton	
Rad. length per module	0.26 %	

Further details can be found in Refs. [1, 6, 7].

3 Electronic Design

The back chamber readout electronics is mounted directly on the long edges of every module opposite to the beam pipes (see Fig. 3). Each electronics board contains 16 preamplifier-shaper-discriminator channels, consisting of a protecting diode, a Fujitsu MB 43468 quad preamplifier, a common-emitter post-amplifier, a fast comparator (MAX 9687), and an ECL gate used as a driver. An external feedback at the comparator stage provides hysteresis of 8 mV to reduce oscillation during the switching. The overall transresistance is 60 mV/μA, given by the 20 mV/μA transresistance gain of the Fujitsu cascade amplifier and an additional factor of three by the post-amplifier.

To ensure electronic stability with the low thresholds required for operation at low gas gain, all possible measures were taken to reduce sensitivity to noise and cross-talk. LCL-filters ensure a clean low voltage, and the threshold control voltage input is attentuated by a factor of 100 by an operational amplifier circuit distributing it to the comparators. The signal cable bundles are shielded to prevent undesired feedback and all parts of the chamber ground system are interconnected without leaving any gaps. Special materials are used to provide good electrical contact free of electrochemical corrosion. These constructions form a high-continuity Faraday cage and provide a common ground, especially for the front-end electronics and the high voltage input. This is important to prevent this system of 7680 channels from oscillating at low threshold values. At a voltage as high as 1800 V (above normal operating values), the chambers exhibit a dark current less than the readout sensitivity limit of 0.1 μA per plane. This behaviour is reflected in the fact that there are almost no hot wires producing fake signals, and that the dark rates agree with the expected cosmic ray background.

Using rather low threshold values yields better resolutions as walk degrades the resolution for higher thresholds. This can be seen in Fig. 4 where three typical pulses are shown. The two horizontal lines indicate typically used threshold values. Although even lower threshold values can be achieved, they are not used, as crosstalk then would cause fake hits, increasing the data volume and cost of event reconstruction. The crosstalk rate for low thresholds can be explained using the BC raw signal amplitude distribution and the coupling between the

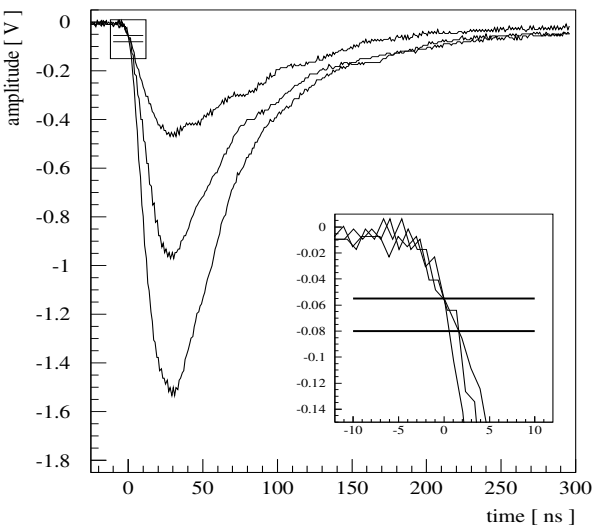

Figure 4: Typical pulses and threshold values.

channels given by the quad preamplifier properties [8, 9]. As a compromise, intermediate threshold values were chosen, typically around 50 mV corresponding to an initial current of 0.8 μA, or a charge of roughly $\sim 5.5 \cdot 10^4$ electrons. At these threshold values and high voltages of typically around 1770 V used in the experiment, inter–plane crosstalk does not play any role.

Another possible impact on the quality of the data is crosstalk on the 30 m long flat twisted pair cables running from the preamplifier boards to the LeCroy 1877 FASTBUS TDCs located in the HERMES electronics hut. The propagation times are perturbed by less than 1 ns when all channels in a plane produce signals at the same time. This is the situation for test pulse measurements but not for physics events. Furthermore the routing of the ribbon cables is done in a way providing maximal spatial distance between those channels that usually fire simultaneously. Therefore, this effect is negligible.

The preamplifiers dissipate 400 W for the smaller and 600 W for the bigger drift chamber modules, requiring efficient cooling. This is provided by 9 big fans for each BC1/2 and 10 for each BC3/4 module. The temperature difference between the upper and lower parts of the steel frame stays below two degrees. Different parts of the steel frame exhibit slightly different thermal expansions due to this temperature gradient. The gas temperature also differs between inlet and outlet, which in principle could affect the Space-Drift-Time-Relation (SDTR). However, neither of these thermal effects degrade the chambers' resolution significantly.

4 Gas Properties

All drift chamber modules of the HERMES spectrometer (see Fig. 1), including the BCs, are operated with the same non-flammable gas mixture consisting of Ar(90 %), CO_2(5 %) and CF_4(5 %). Mixtures containing CF_4 have been shown to result in compromised resolution due to electron attachment [10]. However, they have the advantages of short occupation time and long chamber lifetime [11]. The properties of this gas mixture were measured with a small single-cell drift chamber designed to study drift velocities and gas gain under varying conditions, including changes in gas composition, gas contamination by N_2 and variations in temperature and pressure [12]. The measured drift velocities v_{drift} vary between 20 and about 70 μm/nsec, at reduced fields ranging between 0.15 and 1.0 V/cm/mbar. They agree rather well with the results from simulations [13] as can be seen in Fig. 5.

Both CO_2 and CF_4 are used as quencher gases to absorb UV photons while reducing the mean energy of the drifting electrons. The cross sections for rotational and vibrational states of these gases are high enough to 'cool' the electrons to energies close to the Ramsauer minimum of the elastic cross section for argon, and the gas becomes 'fast' [14]. Especially CF_4 makes the gas fast and helps to

avoid ageing effects [11]. After three years of running no indications of ageing have been observed.

The gas system supplying the drift chambers with the gas mixture was built at TRIUMF/Canada. The system consists of a mixing station and a recycler with an O_2/H_2O absorber. The composition of the gas, the flow rates through each of the chambers and the recycled fraction are programmable via a series of flow controllers. The gas volume of each chamber is completely exchanged eight times per day. The composition of the outgoing gas is analysed by a Quadrupole Mass Spectrometer. In addition, a small drift chamber is installed in the outgoing gas stream to monitor continously the stability of gas gain and drift velocity [15].

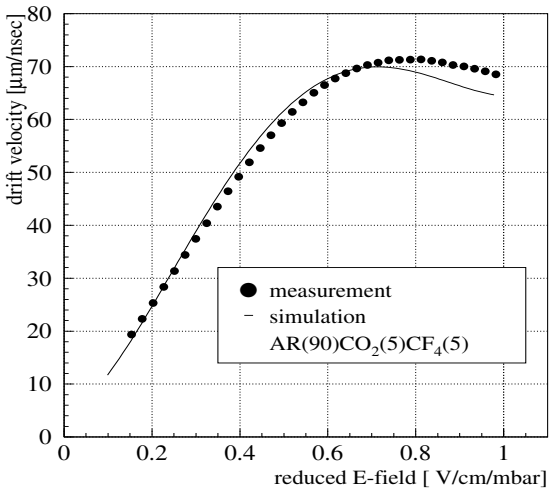

Figure 5: Drift velocity as function of the reduced electrical field.

Due to diffusion through the window foils of the BCs [9] there is contamination of the chamber gas by O_2, N_2 and H_2O, especially when operating the gas system in the recycling mode. Whereas O_2 and H_2O are filtered out by the purifier, the N_2 content depends on the recycled fraction.

The influence of the N_2 contamination on the drift velocity and the gas gain has been measured. An increasing content of N_2 results in only a slight decrease in the drift velocity. The gas gain, however, is strongly reduced as can be seen from Fig. 6 where the dependence of the gas gain on the N_2 admixture is shown for three high voltages. Lower gas gain not only leads to a lower chamber efficiency but also influences the chamber resolution, due to increasing discriminator walk (cf. Fig 4). To prevent performance

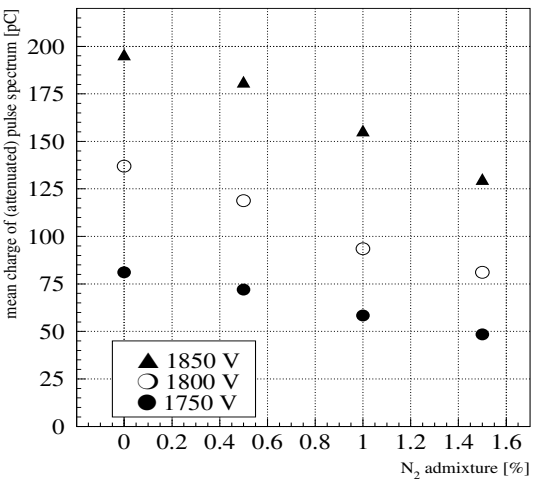

Figure 6: Measured mean gas gain as function of the N_2 admixture at different high voltages. The vertical axis represents the mean values of the spectra from a charge–integrating ADC, and does not represent the absolute gas gain.

deterioration caused by an excessive N_2 contamination, the recycled fraction is set to 80 % (20 % exhaust). This keeps the N_2 contamination stable at a level of 0.4 % with negligible influence on both drift velocity and gas gain (cf. Fig. 6).

5 Alignment and Calibration

A precise measurement of the particles' momentum requires careful alignment and time calibration of all drift chambers involved in the tracking system.

The BC geometrical alignment and time calibration is done in an iterative procedure using reconstructed straight track segments spanning the BC region. These track segments are part of a valid full track. The tracks from all registered particles have been taken into account, which are about 97 % hadrons. From the TDC information and the reconstructed hit position of the track in each chamber plane, the residuals are calculated for the left (r_l) and right (r_r) half of the drift cell separately. For a BC x–plane this is given by the relation:

$$r_{\mathrm{l(r)}} = +(-)\,[x_\mathrm{rec} - x_\mathrm{w}] - \frac{x_\mathrm{d}}{\cos\phi}. \tag{1}$$

where x_w is the position of the wire fired, x_rec is the position of the intersection of the reconstructed track segment with the chamber plane, x_d is the drift distance calculated from the drift time by using the SDTR, and ϕ is the angle of the track in the xz-plane of the HERMES spectrometer (for the HERMES coordinate system see Fig. 3). The sign of the term $[x_\mathrm{rec} - x_\mathrm{w}]$ is *positive* for the left and *negative* for the right half of the drift cell.

From the mean value of these left/right residuals averaged over many tracks, $\langle r_\mathrm{l}\rangle$ and $\langle r_\mathrm{r}\rangle$, the alignment offset δw and the time offset correction δt_0 of the trigger time calibration are calculated according to

$$\delta w = \frac{1}{2}(\langle r_\mathrm{l}\rangle - \langle r_\mathrm{r}\rangle) \tag{2}$$

and

$$\delta t_0 = \frac{1}{2}\frac{\langle r_\mathrm{l}\rangle + \langle r_\mathrm{r}\rangle}{\langle v_\mathrm{drift}\rangle}, \tag{3}$$

where $\langle v_\mathrm{drift}\rangle$ is the average drift velocity.

The calculation can be performed for a single drift cell, i.e. a single wire, or for a whole plane by taking into account all drift cells, i.e. all wires, of this plane. The variables relevant for a whole plane will be denoted with $\overline{\delta w}$, the plane alignment offset, and with $\overline{t_0}$, the plane time offset correction.

In the following subsections the different corrections will be discussed in more detail.

5.1 Alignment

During installation of the HERMES spectrometer, the positions of all detectors were measured by the DESY surveying group using optical triangulation. The accuracy of this method is about 300 μm in the transverse directions, i.e. in x and y, and of order 1.5 mm in the longitudinal direction, i.e. in z. This is not sufficient for the anticipated momentum resolution of the HERMES spectrometer, which requires the knowledge of the detector positions within at least 100 μm. The most important degrees of freedom in the alignment procedure can be divided into two groups:

1. *Transverse alignment correction:* Simultaneous shift, perpendicular to the wire direction, of all wires in a given plane.

   Because of the verified production accuracy of 30 μm for the uniformity of the wire spacing [5], this is the only degree of freedom required for each plane in that coordinate which is in the wire plane, perpendicular to the wires.

   This transverse alignment correction is calculated as the alignment offset $\overline{\delta w}$ from equation (2) by combining all wires in the given plane. The corrected position of the origin of this plane is used in the HERMES geometry database for the next reconstruction cycle. After convergence of these iterations, the position of each plane is determined with an uncertainty smaller than 50 μm.

   Some of these corrections of the individual plane positions can result in an effective movement of the entire module. Especially for the u– and v–planes, an alignment offset perpendicular to the wire orientation is related to a shift in both x and y. Due to the degree of freedom in rotating the chambers around the beam axis, the entire chamber modules are shifted to minimize deviations from the initial optical measurements.

2. *Longitudinal alignment correction:* Shift of a whole BC module in the z–direction.

   For the correction of offsets in the z–position it is necessary to determine the dependence of the apparent x, u or v alignment offsets on the incident track angle. Since alignment was typically done with tracks recorded with magnetic field off, all tracks are straight and point back to the target interaction point. Hence the track angle is almost strictly correlated with the wire number in each plane, so that this angle dependence can not be seen in plane averages. Therefore the aligment offsets must be calculated for each individual wire or, at least, for several groups of wires. The track angle dependence arising from an offset in z is demonstrated in Fig. 7 for one specific plane of the lower BC module B3L. It is clear that, while using

such a track sample, z alignment depends completely on being able to trust the absolute precision of the wire spacing.

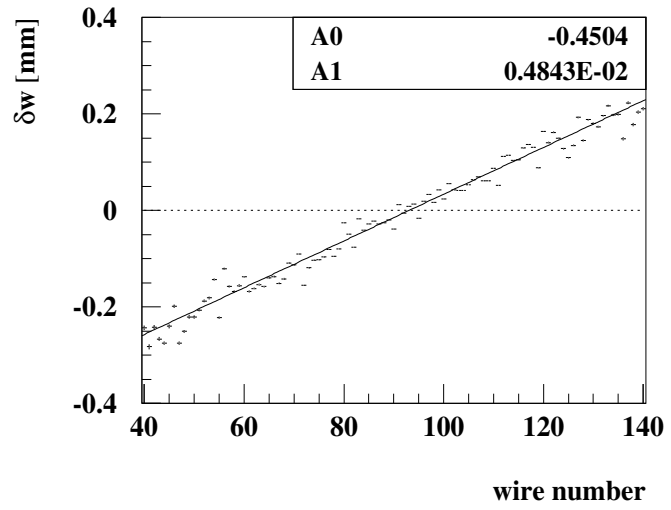

Figure 7: Transverse alignment offset δw vs. wire number for a specific plane of the module B3L located at z = 5.795 m.

The wire numbers are related to x by the wire spacing. Since all tracks come from essentially a point source at z=0, the slope of the fitted line can be represented by the relation $\delta x/x = \delta z/z$. For example, using this relation, a z-shift of δz = 1.87 mm is extracted for the plane illustrated in Fig. 7.

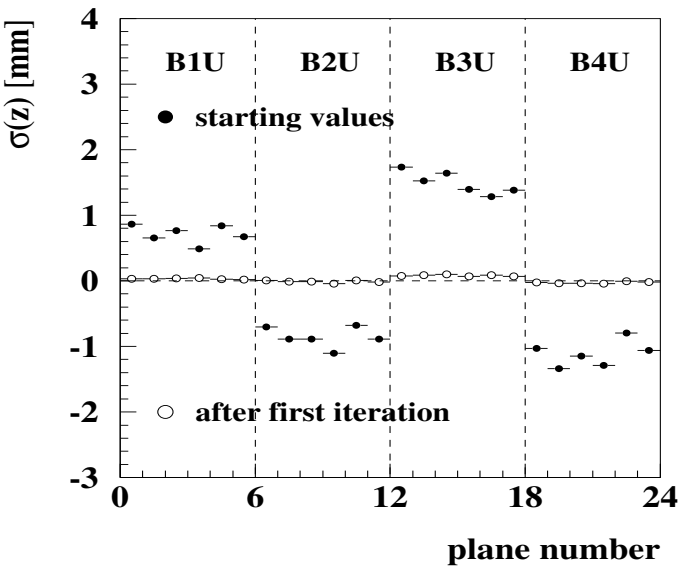

Figure 8: The calculated z–shift for all planes of the upper (B1U-B4U) BC modules. Shown are the starting values (full circles) and the result of the correction after one iteration step (open circles).

For each plane such a z–offset was calculated. The results for the upper (B1U – B4U) BC modules are shown in Fig. 8 for the first two steps in the iteration procedure. The results for the relative z–positions of the individual planes within a chamber module are consistent with design values and

require no adjustment. Hence only a module z–offset was determined by averaging the individual plane z–offsets within a module, and the HERMES geometry database was corrected accordingly for the next iteration. This iterative procedure converges quite fast. Already after the first iteration the remaining z–offsets are below 200 μm (see Fig. 8), and only one further step is necessary to reach the required accuracy.

Alignment corrections due to rotations of individual chamber modules around certain axes have been investigated and are found to be negligible [16]. A relative top/bottom alignment is still under investigation.

5.2 Time Calibration

The signal times from the wires are measured by TDCs in common stop mode. Correspondingly the earliest signal with the shortest drift distance results in the largest TDC conversion value, and the actual drift time is calculated as

$$t_{\mathrm{d}} = t_0 - t_{\mathrm{TDC}}, \tag{4}$$

where t_0 is the trigger time offset depending on the electronics configuration, the cabling, and the trigger arrangement. It must be determined for each channel separately. For a t_0 calibration based on track data, the data from several running periods (i.e. several days) have to be combined to obtain sufficient precision. For those wires near the edge of the acceptance, even the combined data sample did not deliver enough statistics and therefore the test pulse information had to be used to calibrate these wires relative to the inner region of the same plane. Using equation (3) the time offset correction δt_0 is calculated and the corrected t_0 value is loaded into the HERMES calibration database. To check the time stability of the t_0 calibration, the plane averaged time offset correction $\overline{\delta t_0}$ is used. Time variations of the t_0 values are caused either by changes in the hardware, e.g. in the trigger system, or by changes in the running conditions of the chambers, e.g. by variations of the atmospheric pressure.

6 Track Residuals and Resolution

The width of the residual distribution is a measure for the resolution of a chamber plane. The residuals are calculated according to Eq.(1). When quoting properties of the residual distributions no distinction is made between the two halves of the drift cell, i.e. the residual distributions for the left and right half of the drift cell are combined. Residuals calculated for a single drift cell will be denoted by r and those averaged over the whole plane by $\overline{r}$.

To illustrate the relevance of the different alignment and calibration steps discussed in the previous section, a system residual distribution is produced by plotting the residuals calculated for the whole BC system, i.e. for all cells of all

planes of all modules. The width of this distribution, $\sigma(\overline{r_S})$, after each step is shown in Fig. 9. The improvement in width by more than 60 % demonstrates the necessity of the complete alignment and time calibration procedure.

A residual distribution typical for a BC1/2 drift cell is shown in Fig. 10. Aside from the tails, the distribution has the shape of a Gaussian. Fitting its central region ($\pm$500 μm) with a single Gaussian gives a mean value compatible with zero and a width $\sigma(r)$ (see Fig. 10) typical for the BC1/2.

For each BC plane a residual distribution was calculated after having performed all the alignment and t_0 offset corrections. The resulting distributions were then fitted by a Gaussian in the same manner as mentioned above. The widths of the residual distributions $\sigma(\overline{r})$ obtained for the different planes of the upper BC modules under normal running conditions are plotted in Fig. 11. They are in the order of 250 μm for the smaller BC1/2 modules and about 275 μm for the bigger BC3/4 modules. Similar results were found for the lower BC modules.

The width of the plane residual distribution for tracks crossing the plane at an angle below 1° is given in Fig. 12 as function of the drift distance for both the BC1/2 and the BC3/4. The plot was

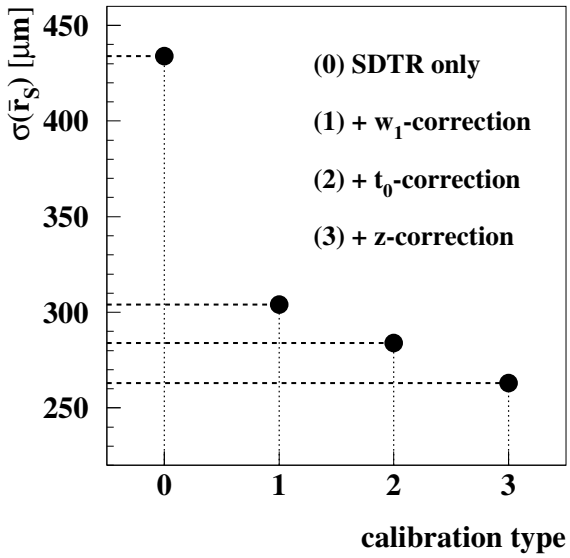

Figure 9: Width of the BC system residual distribution $\sigma(\overline{r_S})$ after the different alignment and calibration steps. The tracks from all registered particles are taken into account.

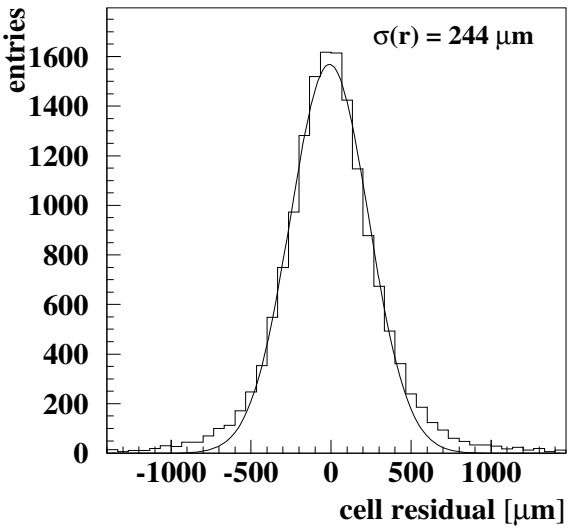

Figure 10: A typical BC1/2 cell residual distribution calculated from the tracks of all registered particles (mainly hadrons). The curve represents a Gaussian fit to the central region ($\pm$500 μm) of the distribution.

obtained by taking into account the tracks of all registered particles and fitting the peak region of the residual distributions with a Gaussian. The tracks close to the sense wire (i.e. small drift distances) were excluded because this region is strongly affected by the difficulties in resolving the left/right ambiguity in this calculation. However, a smooth behaviour of the residual can be assumed. As expected, the best value is measured in the central region of the drift cell to be about 210 μm for the BC1/2 and about 250 μm for the BC3/4. The deterioration of the spatial resolution for tracks near the sense wire (0 mm) is caused by fluctuations of the primary ion-pair production
statistics leading to remarkable drift distance differences and for tracks near the potential wire (7.5 mm) by electron diffusion [17]. In addition, gas mixtures containing CF_4 have been shown [10] to affect the resolution due to electron attachment, which is especially relevant for long drift distances.

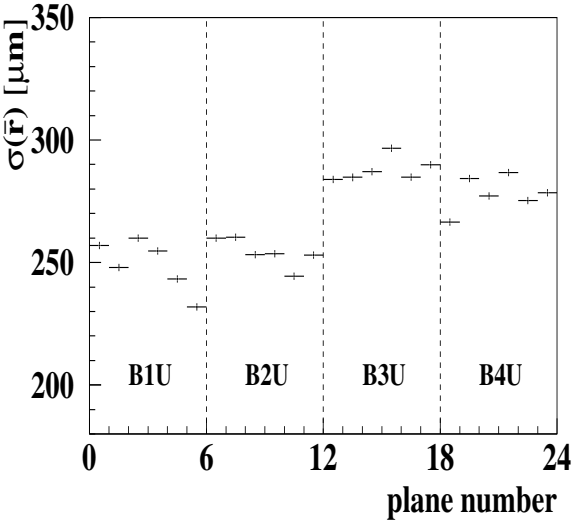

Figure 11: Width of the residual distribution $\sigma(\overline{r})$ of the upper (B1U-B4U) BC planes after all corrections as described in the text.

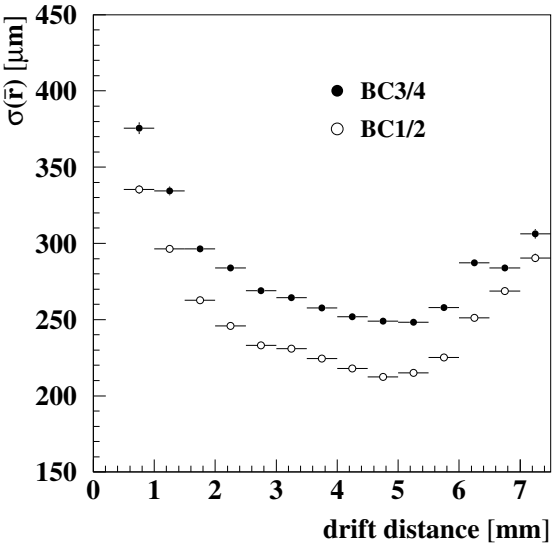

Figure 12: Width of the residual distribution $\sigma(\overline{r})$ of the BC1/2 and BC3/4 as function of the drift distance. All corrections described in the text have been performed.

Using the reconstructed track as reference track for calculating the residual ('internal' method), the spatial resolution of a chamber plane is related to the width of the residual distribution by a geometrical factor that depends on the number of planes of each type and their absolute position in z. This factor varies from plane to plane by a few percent. For the HERMES geometry the resolution of a BC plane is about 10 % bigger

than the width of its residual distribution [18].

For completeness we mention that smaller values for the resolution had been obtained under test beam conditions and using an external reference track defined by a Silicon Microstrip Detector telescope. A value of 150 μm was measured in the central region of the BC drift cell [3, 4]. However, it should be noted that the $e^{\pm}$ momentum resolution in HERMES is almost dominated by bremsstrahlung in the materials of the target cell, the vacuum window, and the vertex chambers (see Fig. 1), and that the spatial resolution of the BCs achieved under normal running conditions is better than required for track reconstruction [19].

7 Plane Efficiency

In the context of this paper the efficiency of a chamber plane is defined as the fraction of reconstructed tracks for which a valid hit from this plane was found in a certain corridor around this track. The corridor width adopted is the same as used in the reconstruction program [19] to find all hits used to reconstruct the track. It is about $\pm$900 μm for the back chamber planes, corresponding to about $\pm 3\ \sigma$, where σ is the plane resolution discussed in the previous section.

Obviously, the results from this definition depends on the reconstruction algorithm. However, it has been checked that this dependency does not introduce any significant bias. It is also obvious that this measure does not account for other inefficiencies in track reconstruction, which might arise from an excessive number of extraneous hits, for example.

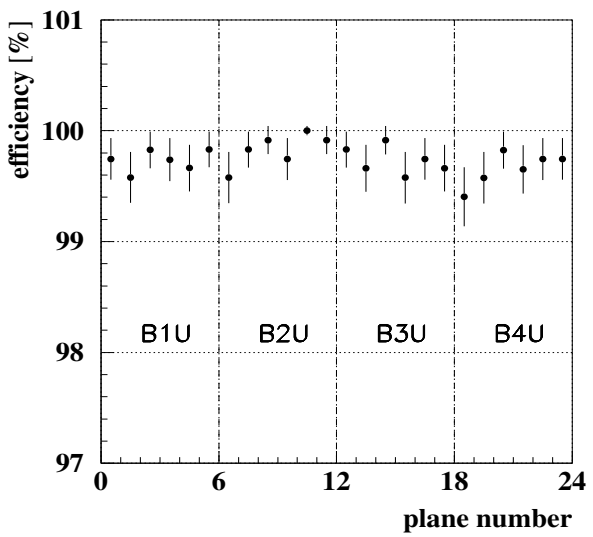

Figure 13: Plane efficiencies of the upper BC modules (B1U – B4U) calculated for electron and positron tracks of one data run.

As a typical example, the plane efficiencies of the upper BC modules are shown in Fig. 13, calculated for all identified electron and positron tracks of one data run. It can be seen that for all planes this efficiency is high and the same within statistical errors. The overall average plane efficiency for those tracks is determined to be well above 99 %. For hadrons a lower efficiency is expected because of their reduced ionization density in the chamber gas compared to electrons and positrons. The efficiency is calculated to be about 97 % using the

tracks of all registered particles, which are mainly hadrons (see Fig. 15).

The dependence of the plane efficiency on the drift distance, averaged over all drift cells of all planes in the upper BC modules, is displayed in Fig. 14. Here a wider corridor than the one mentioned above is used for calculating the efficiencies, namely 1.5 drift cells, and the tracks from all registered particles are taken into account. In the central region of the drift cell the efficiency is high and approaches almost unity, while towards the sense wire (0 mm) and the potential wire (7.5 mm) it falls. This behaviour is well known and can be explained by the same effects as already mentioned in the previous section when discussing the drift distance dependence of the resolution.

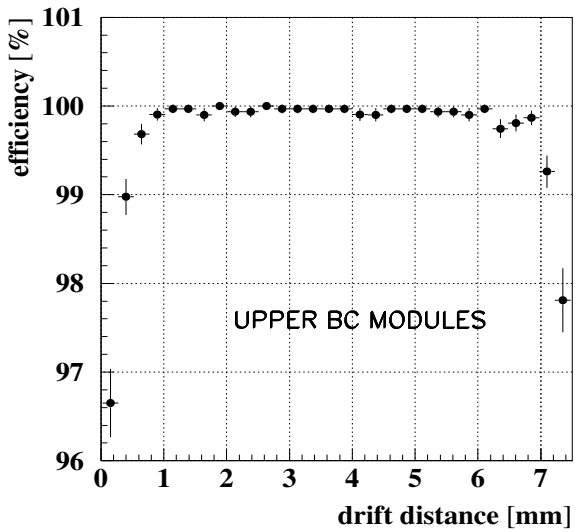

Figure 14: Plane efficiency vs. drift distance for the upper BC modules, calculated for all registered tracks of one data run using a wider corridor for calculating the efficiency than used for Fig.13.

8 Gain Stabilisation and Chamber Performance

On the basis of test run data and the early 1995 data analysis, an optimal set of operating parameters (gas gain and electronic threshold) was initially chosen for HERMES running in order to obtain high efficiency and good resolution at a moderate crosstalk. Studies of the time dependence of calibrations derived from the 1995 data indicate long term stability of the electronics. The expected correlation between the chambers' performance and the atmospheric pressure was also observed [9]. As is well known, an increase in pressure decreases the gas gain and vice versa. This was the reason for introducing in the middle of 1996 running the dynamical high voltage adjustment controlled by pressure measurements. The 'nominal' high voltage setting at normal atmospheric pressure of 1013 mbar was chosen to be 1770 V. In order to keep the gas gain approximately constant during running, the high voltage is adjusted to compensate for the change in atmospheric pessure using a parametrisation given in [20]. The high voltage setting is corrected in steps of 1 Volt over a range of ± 20 Volts, which corresponds to a variation in pressure over a range of ± 30 mbar. This scheme improved the stability of the chamber performance significantly, as illustrated by the reduction of the slope in Fig. 15. The improvement in average efficiencies by 1 to 2 % achieved in 1996

compared to 1995, also seen in Fig. 15, is the result of further optimizing the working conditions. In the HERMES experimental environment, threshold settings at the comparator input of 65 mV for BC1/2 and 80 mV for BC3/4 were found to ensure stable performance at low crosstalk (cf. sect. 3).

The gain stabilization scheme, together with careful alignment and calibration work, resulted in remarkable long term stability of the chamber performance. This can be judged from Fig.16, which shows the behaviour of one specific BC plane over one week of 1997 running. The vertical lines indicate the beam fill boundaries. Typical fills of the HERA storage ring last about 12 hours, separated by several hours for refilling.

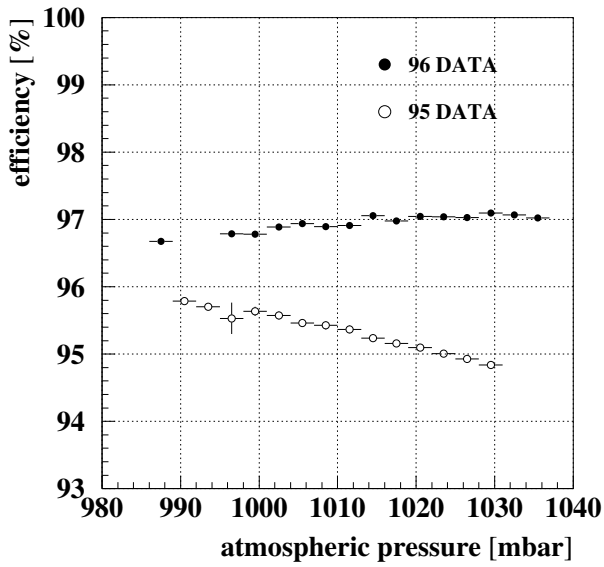

Figure 15: Averaged BC plane efficiency as function of the atmospheric pressure for the 1995 data sample (open circles) and a 1996 data sample after introducing a gain stabilization scheme (closed circles). The efficiency is calculated from tracks of all particles, which are mainly hadrons.

Resolution and efficiency were quite stable over this running period (see Fig.16 a) and b)). The efficiency shown for this particular BC plane turned out to be somewhat higher than the average value for all planes shown in Fig.15. Variations in the atmospheric pressure were checked several times per minute, and the high voltage was adjusted appropriately (see Fig.16 c) and d)). The stability of the electronics and alignment is shown in Fig.16 e) and f). Plotted there are the remaining values deduced from the data for δt_0 (trigger time offset correction) and δw (transverse alignment offset). The t_0 time offsets are calibrated once per fill. As can be seen, their variation is below the level of the 0.5 ns time resolution of the LeCroy 1877 FASTBUS TDCs. The general alignment of the detectors is done only once per year of operation. The residual alignment offsets δw can be used to monitor the stability of the alignment for all runs.

The back chambers have worked without major problems since the commissioning of the experiment in spring 1995. They provided very reliable tracking information for the back region of the HERMES spectrometer. During the first three years of operation, no wire was broken and only one wire lost connection by slipping out of the soldering. This, however, did not degrade the tracking capabilities of the BC system in any significant way because of the high redundancy.

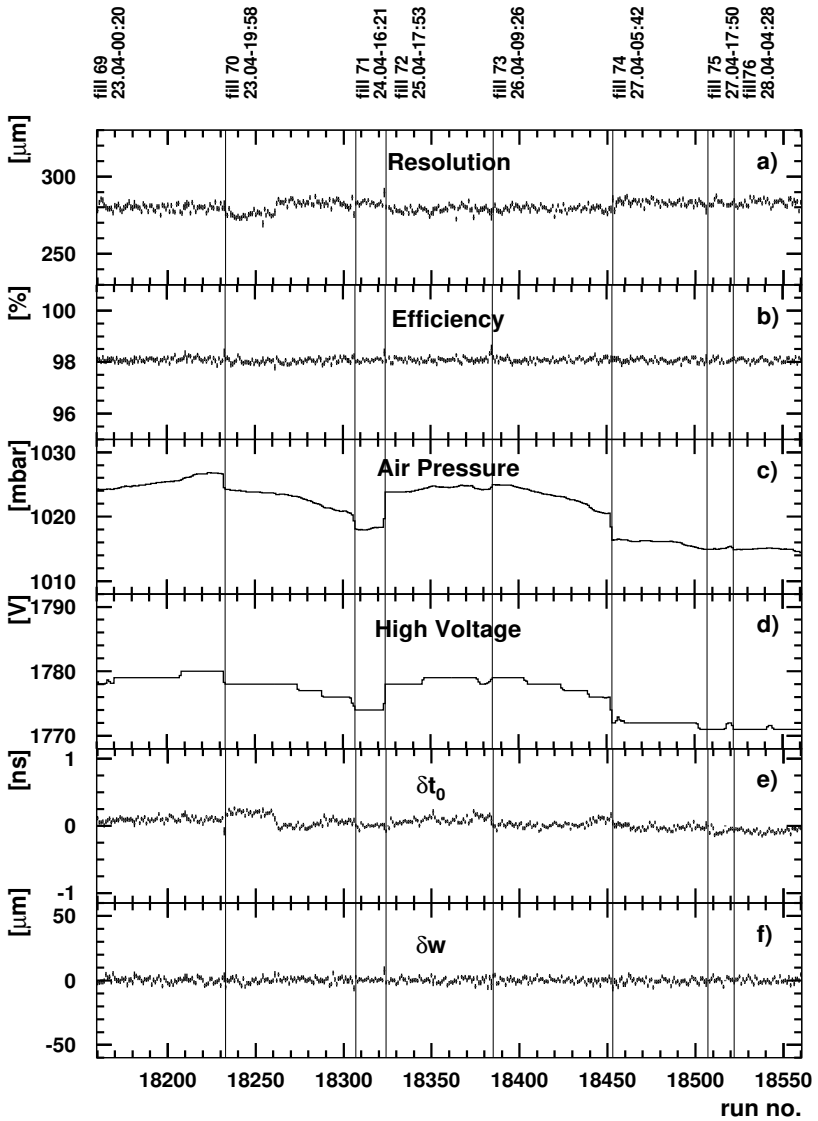

Figure 16: Stability of the back chamber performance. Shown is the typical behaviour of the resolution, the efficiency calculated from tracks of all registered particles (mainly hadrons), the atmospheric pressure, the high voltage, the residual time offset correction δt_0, and the residual transverse alignment offset δw for a specific BC plane over one week of 1997 running. The vertical lines indicate the fill boundaries.

9 Online Monitoring

To operate the BCs with high efficiency during routine operation, it proved essential to have high quality online monitoring and slow control capabilities. One of the event triggers (two tracks from photoproduction) incorporates the x–planes

of the most upstream upper and lower BC modules and thus depends particularly on reliable and stable operation. The low and high voltage supplies are integrated into the HERMES slow control scheme. All voltages are checked several times per minute. Recovery from high voltage trips (typically due to beam anomalies) is automatic. The temperature of the electronics is checked by temperature sensors. All components of the gas system are also accessible to the slow control system, and a special monitor chamber is installed to check continuously the drift velocity and the gas gain. A set of plots of distributions in hit wires and drift times is provided for online checks.

An additional online drift chamber monitor program, based on a simplified track finding algorithm, provides performance information for each chamber module independent of all other detectors [18]. The combination of hits from the six planes of a module is sufficient for the reconstruction of a useful sample of tracks. A measure of the functionality of a module is the number of tracks found using its data alone, compared to the average number of tracks seen by all BC modules. This relative rate is updated and displayed every few seconds to monitor the functionality of the module.

10 Conclusions

The back chamber system proved to be one of the most stable and reliable components of the HERMES spectrometer. After careful alignment and calibration work, the residual distributions of the BCs have a width in the order of 250 μm (σ) for the smaller BC1/2 and 275 μm for the bigger BC3/4 when calculated from the tracks of all registered particles, which are mainly hadrons. The chamber resolution is about 10 % bigger than its residual width due to a geometrical factor given by the HERMES geometry. These numbers are considered to be acceptable in view of the chosen gas mixture containing CF_4, which has shown to result in compromised resolution due to electron attachment. The spatial resolution achieved is better than required for the anticipated $e^{\pm}$ momentum resolution in HERMES, which is dominated by bremsstrahlung. The single–plane detection efficiency for electron and positron tracks is always above 99 %. Gain stabilisation by dynamical high voltage control according to atmospheric pressure leads to very stable operating characteristics such as resolution, efficiency, and calibration.

Finally one can state that in its first three years of running, the back chamber tracking system has met all the requirements of the HERMES experiment.

Acknowledgements: The authors are grateful to C.A. Miller for his continuous support of this project and for many stimulating discussions. We very much appreciated the cooperation of R. Openshaw and M. Kückes concerning the gas

system. We are indebted to our Russian colleagues A. Laritchev, M. Negodajev, W. Kozlov, and S. Orfanitzky for their help during the assembly phase of the chamber construction. Finally, we gratefully acknowledge the skillful and enthusiastic work of the mechanical and electronics workshops in Erlangen and Zeuthen, which was absolutely essential to build the whole system with high quality and according to the schedule.

References

[1] HERMES Collaboration, Technical Design Report, DESY-PRC 93/06 (1993),
HERMES Collaboration, 'The HERMES Spectrometer', to be submitted to Nucl. Instr. and Methods A.

[2] HERMES Collaboration, 'The HERMES Internal Gas Target', to be submitted to Nucl. Instr. and Methods A.

[3] S. Bernreuther et al., Nucl. Instr. and Methods A367 (1995) 96.

[4] D. Hasch, Diploma thesis (1995), Humboldt – Universität zu Berlin.

[5] A. Gute, Diploma thesis (1994), Universität Erlangen–Nürnberg.

[6] S. Bernreuther, Diploma thesis (1995), Universität Erlangen–Nürnberg.

[7] F. Neunreither, Ph.D. thesis (1997), Universität Erlangen–Nürnberg.

[8] H. Russo, Diploma thesis (1996), Universität Erlangen–Nürnberg.

[9] W.A. Lachnit, Ph.D. thesis (1998), Universität Erlangen–Nürnberg.

[10] S.F. Biagi, Nucl. Instr. and Methods A310 (1991) 133.

[11] R. Openshaw et al., Nucl. Instr. and Methods A307 (1991) 298.

[12] F. Schmidt, Diploma thesis (1996), Universität Erlangen–Nürnberg.

[13] S.F. Biagi, MAGBOLTZ Program version 2.2 (1990), Univ. Liverpool.

[14] L.G. Christophorou et al.,Nucl. Instr. and Methods A163 (1979) 141.

[15] A. Buchsteiner, Diploma thesis (1996), Humboldt – Universität zu Berlin.

[16] Y. Gärber, Diploma thesis (1996), Humboldt – Universität zu Berlin and private communication.

[17] N.A. Filatova et al., Nucl. Instr. and Methods 143 (1977) 17; F. Sauli, CERN 77-09 (1977).

[18] F. Meißner, Diploma thesis (1995), Humboldt – Universität zu Berlin.

[19] W. Wander, Ph.D. thesis (1996), Universität Erlangen–Nürnberg.

[20] J.C. Armitage et al., Nucl. Instr. and Methods A271 (1988) 588.